scientific reports

Check for updates

OPEN

Effect of ultrasonic atomization parameters on AlSi12 aluminum powder characteristics for additive manufacturing

Andrei Yankin[1], Hussain Ali Murtaza[2], Boris Golman[2], Asma Perveen[1] & Didier Talamona[1]✉

The adoption of additive manufacturing (AM) has driven extensive research into metal feedstocks, uncovering strong links between powder quality and the performance of printed parts. Poor powder characteristics, inadequate flowability or inconsistent packing, can significantly degrade the mechanical performance of the final 3D-printed components. This study investigates the effects of arc manipulator angle, electrical current, and vibration amplitude on AlSi12 powder quality via ultrasonic atomization (UA). Parameter adjustments significantly influenced particle size distribution, with span variations up to 37.5%. Optimal rheological properties were achieved by increasing the vibration amplitude (from 75 to 80%), decreasing the arc angle (from 5° to -5°), and reducing the current (from 150 A to 140 A). A modified AM suitability factor (AMS) was developed, incorporating logarithmic transformation and custom weighting to mitigate high-uncertainty parameter effects. Results revealed a non-linear relationship between powder suitability and arc angle, with a sharp worsening above 0°. Electrical current had the greatest impact on powder quality, followed by arc angle and vibration amplitude. Benchmarking showed that UA powder achieved suitability factors 21% higher than commercial powder, with improved sphericity compared to the irregular, fused particles of commercial alternatives. These findings underscore the potential of UA to enhance AM part reliability.

Keywords Ultrasonic atomization, Metal 3D printing, Additive manufacturing suitability factor, AlSi12 aluminum alloy, Rheological properties, Particle size distribution

Aluminum alloys are the main structural materials, whether in aerospace, automotive, or general manufacturing, thanks to their outstanding corrosion resistance, thermal conductivity, fatigue behavior, and overall strength-to-weight ratio[1–3]. In particular, alloys such as AlSi10Mg, AlSi12, and AlSi7Mg have been utilized for AM, enabling the production of intricate geometries and topology-optimized components that would be extremely challenging or outright impossible to fabricate using conventional methods[4–6].

Hereby, the field of metal additive manufacturing (AM) is gathering increasing attention from both academic researchers and industries such as aerospace, defense, biomedical, and conventional manufacturing[7–9]. This growing interest has spurred numerous studies focused on uncovering the intricate relationships between powder properties and the quality of 3D-printed components[10–12].

The flow and packing characteristics of metal powders are crucial for both process efficiency and final product quality[13–15]. Research indicates that although a broader particle size distribution (PSD) can enhance packing density, it may simultaneously reduce flowability[15,16]. Particle size can also influence the solidification behavior of powders, thereby affecting their microstructure and microsegregation[17]. Furthermore, particle shape can affect flowability and powder spreading. For instance, elongated particles tend to reduce powder quality due to frequent force-arch formation and wall effects, resulting from strong particle interlocking[18]. These features, in turn, have significant importance to the mechanical properties of the final consolidated bulk materials.

Metal powders are utilized in a wide range of applications, including AM and thermal sprayed coatings[19]. The powders are produced through various methods, including mechanical, chemical, and physical processes. Among these techniques, atomization stands out as a well-established and widely used method. This process involves the transformation of molten metal into liquid droplets, making it a crucial step in the production of high-quality metal powders[20].

[1]Department of Mechanical & Aerospace Engineering, School of Engineering and Digital Sciences, Nazarbayev University, Astana, Kazakhstan. [2]Department of Chemical and Materials Engineering, School of Engineering and Digital Sciences, Nazarbayev University, Astana, Kazakhstan. ✉email: didier.talamona@nu.edu.kz

Powder atomization utilizes various technologies, including gas atomization, water atomization, plasma atomization, etc[21,22]. The primary goal of these methods is to produce high-quality powders that exhibit the desired properties and performance characteristics necessary for achieving optimal results in AM. Meanwhile, researchers frequently investigate how different atomization parameters influence the resulting powder characteristics[23–25]. The atomization techniques mentioned above may encounter several challenges. For instance, gas atomization often faces issues such as the formation of satellite or porous particles[26,27]. Water atomization poses a challenge due to the increased surface oxide content in the produced powders[28]. It can result in various defects in the final product[29].

Ultrasonic atomization (UA) is one of the least explored methods for atomizing metal melts[30]. This technique employs ultrasonic vibrations to convert molten metal into fine droplets[31–33]. The UA method has the potential to produce high-quality powders with exceptional properties, which may significantly enhance the quality of the final 3D-printed product. While UA demonstrates material utilization efficiency comparable to that of gas atomizers, with more than half of the produced batch meeting AM requirements, it remains a relatively new technology for small—to medium-scale production[30,34]. Initially, this method was primarily applied to materials with low liquidus temperatures, such as solders. However, recent research has expanded its application to metals with higher melting points[30].

Continuous UAs of Al melts require substantial ultrasonic amplitudes due to the metal's low density and the fast oxidation of droplets[29]. Spherical micro powder of pure aluminum and Al-Si alloy were successfully fabricated using ultrasonic-assisted atomization, achieving a minimum particle diameter of approximately 15 μm in[35]. Additionally, the powdering of Al, Al/Sn, Al/Pb, and Al/Al_2O_3 alloys is detailed in[36]. Shabana et al.[37] present an effective method for producing aluminum nanoparticles using ultrasound, achieving an average particle size of around 13 nm.

Jedynak[38] demonstrated the production of an AlSi9Mg aluminum alloy reinforced with 20 vol% SiCp through UA technology using the ATOLab + system. The process utilized fixed parameters, including a vibration frequency of 35 kHz, an amplitude of 80%, and an arc electrical current of 130 A. Meanwhile, Monti et al.[39] introduced a new Al-5.0Cu-3.0Ti-1.5Cr-1.3Fe alloy manufactured using Laser Powder Bed Fusion (LPBF). The powder was produced with the ATOLab + ultrasonic atomizer, operating at frequencies around 35 kHz and vibration amplitudes between 65% and 75%. This process enabled the fabrication of crack-free samples with a density of 99.2% and hardness values surpassing those of conventional aluminum alloys.

To date, only a limited number of studies have focused on the investigation of UA aluminum alloy powders. Furthermore, to the best of our knowledge, no literature has explored AlSi12 powder produced using the UA technique. As previously mentioned, AlSi12 is an often-used alloy in metal AM, particularly for aerospace, automotive, and other applications, due to its excellent mechanical properties. Additionally, there is a gap in research regarding how UA process parameters affect the quality of aluminum powders. This work aims to address these gaps by exploring the novel application of UA for AlSi12 powder and benchmarking its characteristics against a conventionally produced powder. It also examines the impact of key atomization process parameters — such as electrical current, amplitude, and electric arc position — on the morphology, PSD, and rheological properties of AlSi12 powder.

Materials and methods

Production of AlSi12 powder by UA method

The AlSi12 powder was produced using an ultrasonic atomizer (ATO Lab + US35). The source material, AlSi12 wire, was obtained from Alunox Schweißtechnik GmbH. The UA process involves several key steps. Initially, the AlSi12 wire is introduced into the system near an electric arc, which heats the material, creating a molten metal pool on a vibrating platform. Ultrasonic vibrations are then applied to the molten metal, causing it to spread into fine droplets that solidify into powder. The resulting metal powder is subsequently collected in a designated powder container.

The atomizer can directly manage several independent parameters. For example, the metal wire is fed into the atomization chamber at adjustable speeds, ensuring the right material quantity on the platform for optimal atomization. Additionally, the welding torch's electrical current can be varied to control the melting temperature and overall process efficiency. The ultrasonic frequency system allows for the control of vibration amplitude, enhancing atomization efficiency. Moreover, the welding torch manipulator enables adjustment of the electric arc position relative to the atomization platform, thereby altering the angle at which molten droplets are dispersed through the chamber into the powder collection container. This angle can be varied from − 5° to 5° relative to the electrode axis. For a more detailed description of the process, see references[40,41]. An overview of the production setup is shown in Fig. 1.

The atomizer is designed to control various operational parameters, including electrical arc (torch) position, electrical current, ultrasonic vibration amplitude, among others. Initially, the electrical current and ultrasonic vibration amplitude were varied to determine their optimal values based on powder rheological properties. After identifying the optimal current and amplitude, the best torch position angle was determined under these conditions (see Fig. 1). Operating parameters are also listed in Table 1.

All powders were sieved through a 63 μm mesh. In our study, only particles smaller than 63 μm were considered suitable for use with the Renishaw AM400 selective laser melting (SLM) system in our laboratory; larger particles were classified as waste. Notably, different metal AM processes may require different particle size distributions, so the definitions of acceptable and waste fractions can vary depending on the application. As a result, around 75% of the produced powder was successfully converted into usable metal powder.

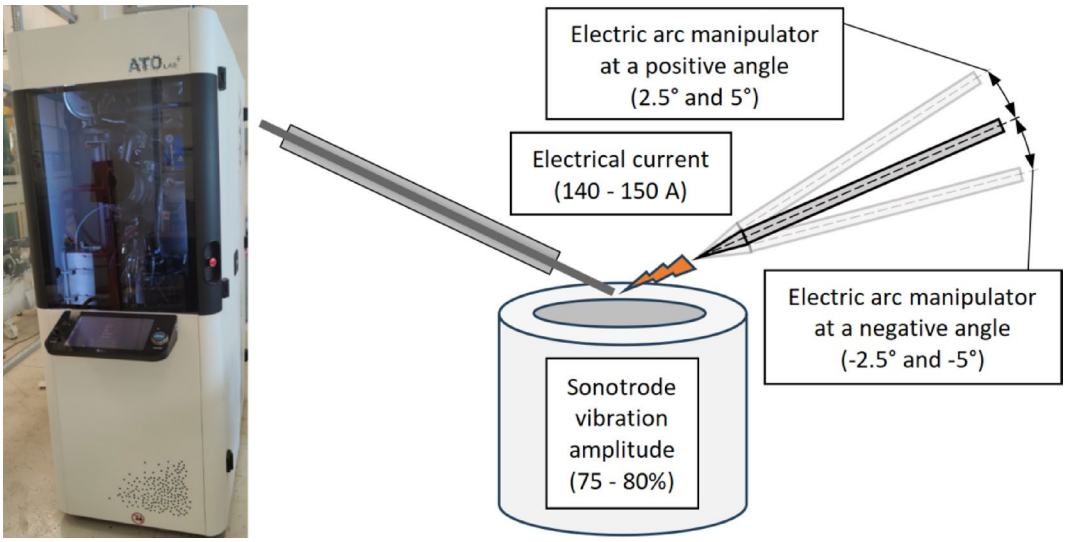

Fig. 1. Production of metal powder using UA ATO Lab + US35 under varying process parameters.

No.	Electrical current, A	Vibration amplitude, %	Electric arc manipulator position, deg	Vibration frequency, kHz
1	140	75	0	35
2	140	80	0	35
3	150	80	0	35
4	140	80	−5	35
5	140	80	−2.5	35
6	140	80	2.5	35
7	140	80	5	35

Table 1. Operating parameters of UA.

Evaluation of powder characteristics

The powder morphology was analyzed using a Scanning Electron Microscope (SEM), JSM-IT200 LA (JEOL). This SEM system also integrates X-ray Energy Dispersive Spectroscopy (EDS) for comprehensive elemental analysis.

The laser diffraction method was used to determine the volume-based particle size distributions of the metal powders, utilizing a Mastersizer 3000 analyzer (Malvern) in compliance with the ISO 13320:2009 standard. Every powder sample was subjected to a minimum of three measurements. The mean values for the D_{10}, D_{50}, and D_{90} provided a detailed description of the PSD. These percentile values represent the particle sizes below which 10%, 50%, and 90% of the total volume of particles are found, respectively. The width of the distribution was measured by the span *S*, defined by Eq. 1[42]:

$$S = \frac{D_{90} - D_{10}}{D_{50}} \tag{1}$$

The rheological properties of the powders were evaluated using a FT4 powder rheometer (Freeman Technology) in accordance with ASTM D8328, D8327. Five distinct experimental methods were employed in this analysis: dynamic flow, aeration, compressibility, permeability, and shear testing[43]. To ensure reliable results, each testing mode was conducted in triplicate using different powder samples. The rheological testing resulted in the measurement of seven key properties: Basic Flow Energy (BFE), Specific Energy (SE), Conditioned Bulk Density (CBD), Aeration Energy (AE), Compressibility Index (CI), Pressure Drop (PD), and Cohesion Coefficient (c).

BFE is measured in the seventh cycle when the test blades move downward, whereas SE is recorded as the blades rotate upward during low-shear blending. Lower values of both BFE and SE correspond to improved powder flowability. CBD denotes the conditioned bulk density of the powder bed, indicating how densely the powder packs. The aeration test evaluates how introducing air alters powder behavior by comparing its flowability before and after aeration; the primary output of this test is the AE. For compressibility, compressive loads are applied progressively using a vented piston, and the resulting decrease in powder bed volume under load is recorded. From these data, the CI is computed as the ratio of the powder bed's density after compression to the CBD measured before compression. The permeability test measures how readily a powder bed releases trapped air. Air is injected at the base of the powder column while a vented piston applies incremental compressive

loads. The resulting air pressure is recorded against each load, and the PD is calculated. Next, the FT4 powder rheometer gauges the shear stress required to initiate powder flow under consolidation, yielding the cohesion coefficient (c). For more information on FT4 powder rheometer testing modes, refer to published materials, such as[44,45].

Results and discussion

UA process parameters

The PSD parameters, including D_{10}, D_{50}, D_{90}, and span values, were evaluated under different conditions of electrical current, vibration amplitude, and torch (electric arc manipulator) positions, as shown in Fig. 2. The D_{10} values showed a consistent decline with increasing torch angles from −5 to 5 degrees. Specifically, the D_{10} values can be grouped as follows: approximately 44–45 µm at −5 and −2.5 degrees, around 43 µm at 0 and 2.5 degrees, and about 41 µm at 5 degrees.

Unlike D_{10}, the D_{50} values did not follow a similar trend, remaining stable between 54 and 55 µm for torch angles from −5 to 2.5 degrees. A significant reduction in D_{50} was observed at 5 degrees, dropping to 52.3 µm. The D_{90} parameter exhibited an increase from approximately 66 to 70 µm when the torch angle changed from −5 to 0 degrees, followed by a decrease back to the initial 66 µm as the angle progressed from 0 to 5 degrees. Due to the variations in D_{10}, D_{50}, and D_{90}, the span values also changed: from −5 to −2.5 degrees, the span remained around 0.4, whereas from 0 to 5 degrees, it increased to approximately 0.5.

Regarding the influence of electrical current, increasing the current from 140 to 150 A led to a statistically significant decrease in both D_{10} and D_{50} values, an increase in span, and no noticeable change in D_{90}, as confirmed by t-tests. In contrast, an increase in vibration amplitude resulted in higher D_{10} and D_{50} values, while span and D_{90} remained statistically insignificant.

Overall, D_{10} values range from 38.7 to 44.7 µm, showing a variation of 13.5%. D_{50} values exhibit a smaller variation, ranging from 52.3 to 54.7 µm (4.4%), while D_{90} values vary from 66.4 to 72.7 µm, representing an 8.7% change. The span, however, shows the most significant variation, ranging from 0.40 to 0.64 (37.5%). Notably, while D_{10}, D_{50}, and D_{90} vary moderately, the span differs much more significantly. As highlighted in references[15,16], particle size parameters can influence powder flow behavior, suggesting that changes in UA process parameters can notably impact this behavior.

The observed trends in PSD parameters can be related to several combined factors governed by process parameters. For instance, the torch angle regulates both the electric arc's trajectory and the argon gas flow direction, which collectively influence heat distribution, melt pool area, and gas-induced droplet dynamics. A reduced torch angle affects the molten material more tangentially, while a larger angle directs the arc more centrally into the melt pool, increasing the localized energy density. Moreover, increasing the electrical current also raises the heat input, resulting in higher melt pool temperatures. Elevated molten metal temperatures lower both viscosity and surface tension, promoting the breakup of the molten stream into finer droplets in the lower regions of the PSD[46,47].

The direction of the argon gas flow, in turn, can influence PSD parameters. At smaller torch angles, powder tends to disperse more tangentially, whereas at larger angles it is directed more centrally, potentially leading to finer particles[48,49]. This suggests that in the UA process, higher torch angles and increased electrical current may contribute to smaller particle sizes, with the effect being more pronounced for finer fractions (e.g., D_{10}).

Additionally, increasing the vibrational amplitude raises the energy input, enabling the formation of larger droplets compared to conditions with lower energy. This can be explained by the higher amplitude increasing the height of capillary waves, thus enlarging the volume of liquid at each wave peak. This may lead to droplet collisions and coalescence, resulting in the formation of larger particles[47].

Figure 3 presents SEM micrographs of AlSi12 powders produced under various process parameters. Figures 3a and 4b show powders obtained at 140 A and 75% amplitude with a torch position of 0°, and at 150 A and 80% amplitude with a torch position of 0°, respectively. Figures 3c and 4g illustrate the effect of torch angle on powder morphology for samples produced at 140 A and 80% amplitude, with torch angles of −5°, −2.5°, 0°, 2.5°, and 5°, respectively. In Fig. 3, blue arrows indicate the increase in torch angle from −5° to 5°, while gray arrows represent the decrease in amplitude from 80 to 75% and the increase in current from 140 A to 150 A.

The images in Fig. 3 reveal that the powders predominantly consist of highly spherical particles, a characteristic that is highly favorable for AM applications[18]. However, a slight increase in particle surface roughness is observed with higher electrical current and at torch angles above 2.5°, which can be attributed to elevated process temperatures. As previously mentioned, increased current and torch tilt can raise the thermal energy in the system, potentially leading to less uniform droplet solidification and rougher particle surfaces. Nevertheless, the majority of particles maintain a spherical morphology, with a notably low presence of smaller satellite particles adhering to the surfaces of larger core particles.

The presence of irregularly shaped, elongated particles, or those exhibiting high surface roughness and satellite formations, adversely affects powder quality. For instance, increased surface roughness enhances interparticle cohesion, thereby reducing flowability, spreadability, and packing density[50]. Similarly, powders with low circularity demonstrate reduced flowability, poorer layer density, increased delamination risk, and greater part porosity during AM processes[51]. Satellite particles degrade flowability and create interparticle gaps within the powder bed[52].

Figures 4, 5, 6, 7, 8, 9 and 10 illustrate the rheological parameters of various powders measured using the FT4 rheometer. The results indicate a decrease in the CBD from 1.064 g/cm³ to 0.957 g/cm³ as the arc manipulator angle increases, representing a reduction of approximately 10% (Fig. 4a). Similarly, an increase in electrical current negatively impacts the CBD, causing a decline from 1.017 g/cm³ to 0.974 g/cm³, equating to a 4% drop (Fig. 4b). In contrast, variations in vibrating amplitude exhibit a minimal effect on CBD, suggesting it is not a significant factor in altering bulk density (Fig. 4c). CBD reflects the bulk density of the conditioned powder bed

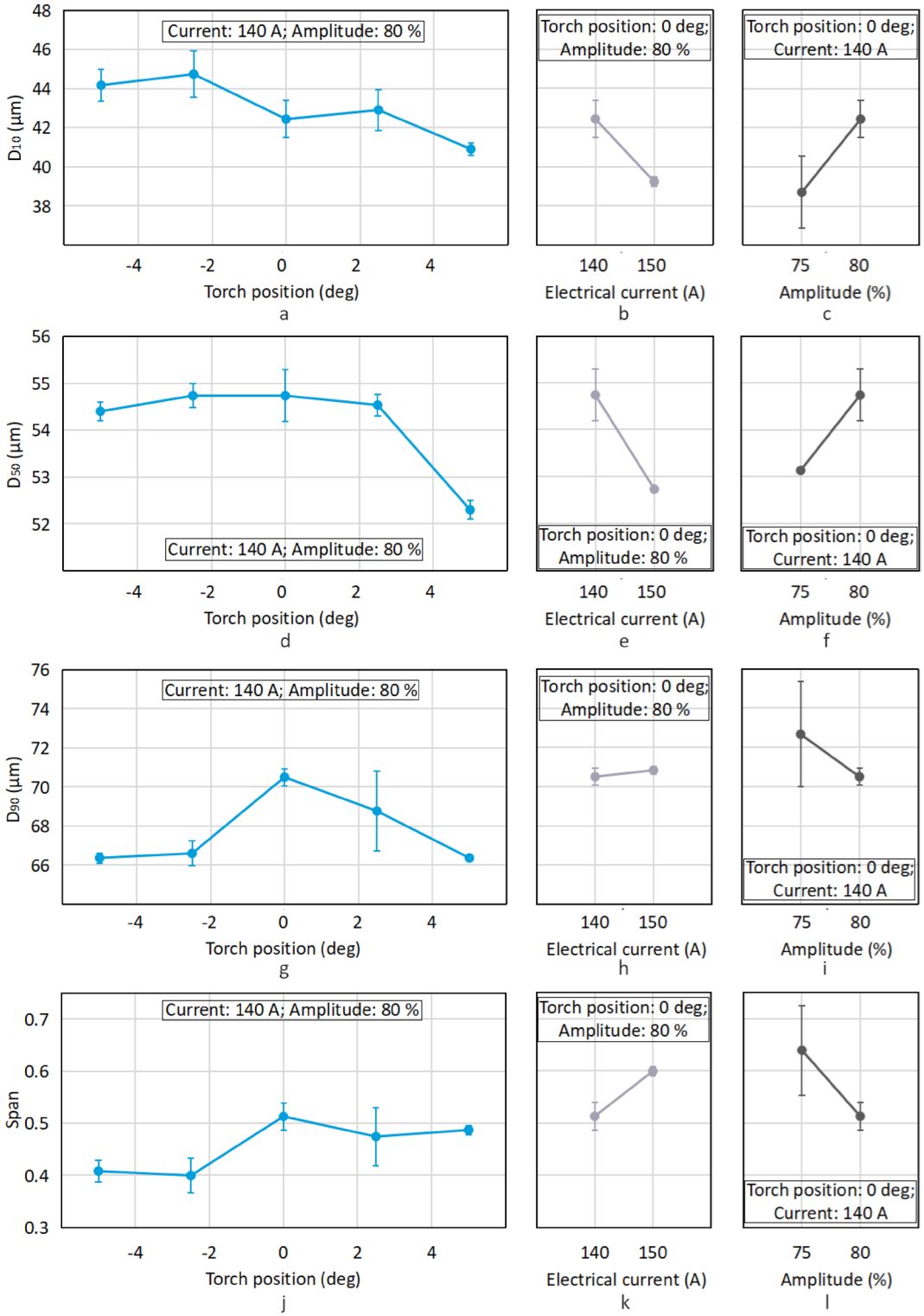

Fig. 2. PSD parameters for AlSi12 UA powder including D_{10} (**a**, **b**, **c**), D_{50} (**d**, **e**, **f**), D_{90} (**g**, **h**, **i**), and S (**j**, **k**, **l**) at varying arc manipulator (torch) angles (**a**, **d**, **g**, **j**), electrical currents (**b**, **e**, **h**, **k**), and vibration amplitudes (**c**, **f**, **i**, **l**).

and is influenced by multiple factors, including particle size distribution, shape, surface texture, and others[53]. The findings underscore that process parameter variations can influence CBD; however, the observed changes are relatively small, with all variations remaining within a 10% range.

The CI reflects the powder's ability to reduce its volume under compression, indicating its compressibility. A higher CI suggests that more air is trapped within the powder[54]. As shown in Fig. 5, CI remains relatively

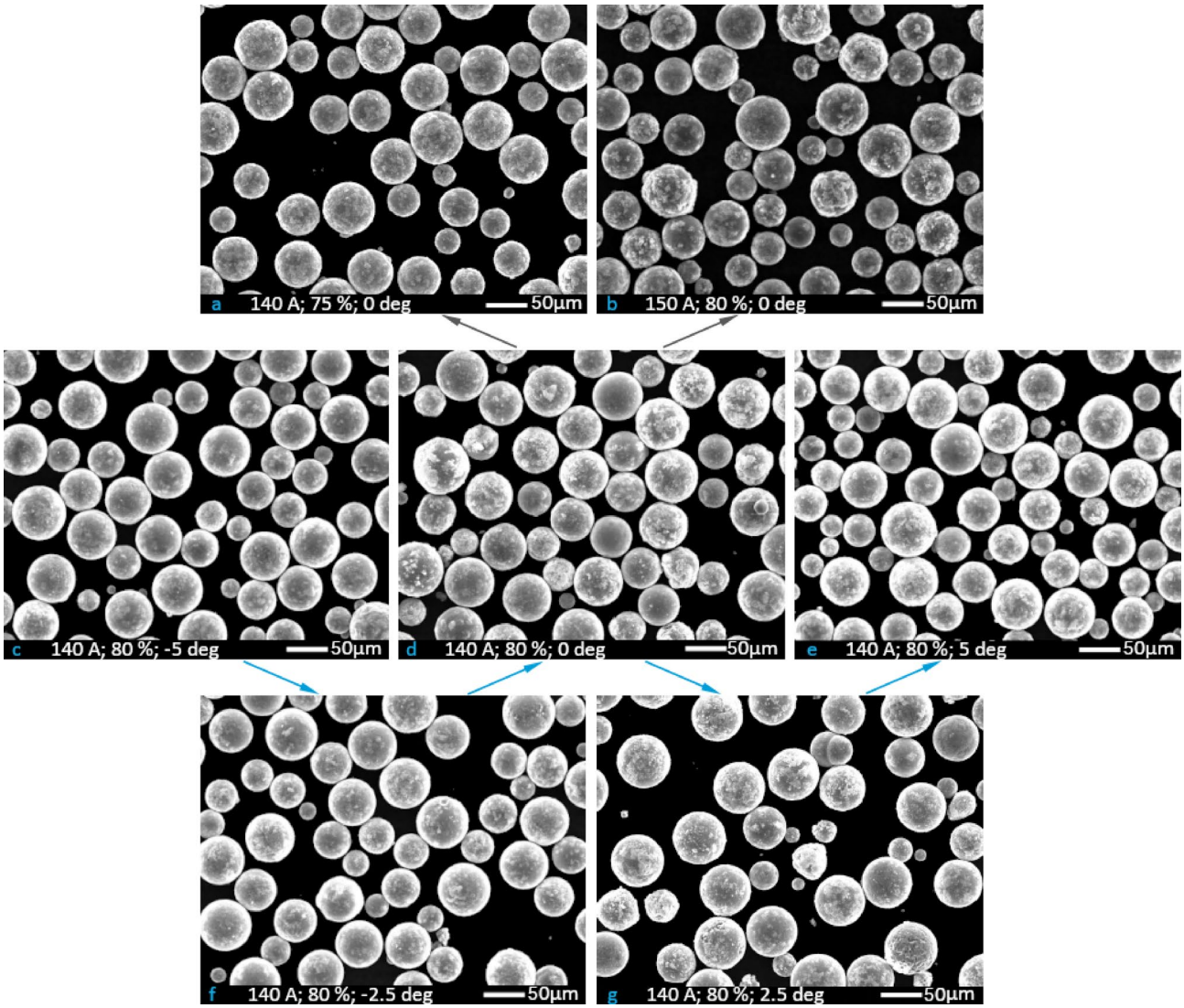

Fig. 3. SEM micrographs of AlSi12 UA powder at varying arc manipulator (torch) angles (**c**, **d**, **e**, **f**, **g**), electrical currents (**b**, **d**), and vibration amplitudes (**a**, **d**).

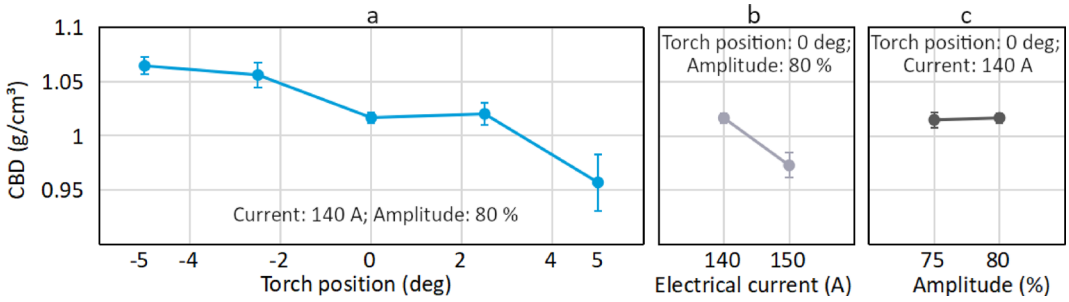

Fig. 4. CBD of AlSi12 UA powder at varying arc manipulator (torch) angles (**a**), electrical currents (**b**), and vibration amplitudes (**c**).

stable when the torch angle varies from − 5 to 0 degrees. However, it begins to increase significantly beyond this range, rising from 2.73 to 3.57% at an angle of 5 degrees. A similar trend is observed with the electrical current, where CI reaches 3.94% (Fig. 5b). In contrast, changes in vibrating amplitude have minimal influence on CI, much like the trends observed with CBD, suggesting it is not a critical factor (Fig. 5c). Notably, CI exhibits

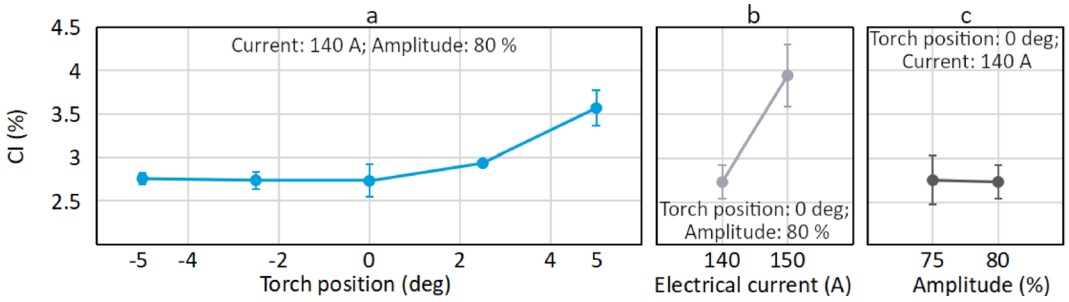

Fig. 5. CI of AlSi12 UA powder at varying arc manipulator (torch) angles (**a**), electrical currents (**b**), and vibration amplitudes (**c**).

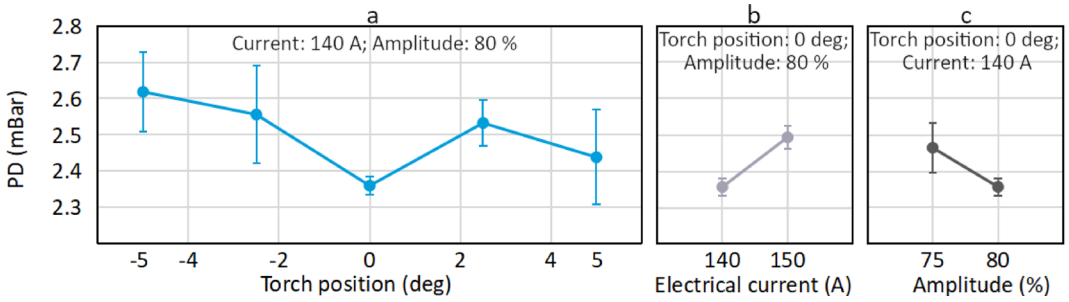

Fig. 6. PD of AlSi12 UA powder at varying arc manipulator (torch) angles (**a**), electrical currents (**b**), and vibration amplitudes (**c**).

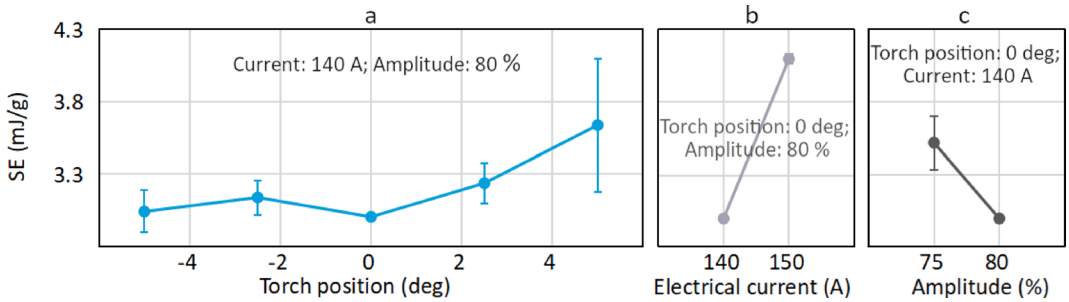

Fig. 7. SE of AlSi12 UA powder at varying arc manipulator (torch) angles (**a**), electrical currents (**b**), and vibration amplitudes (**c**).

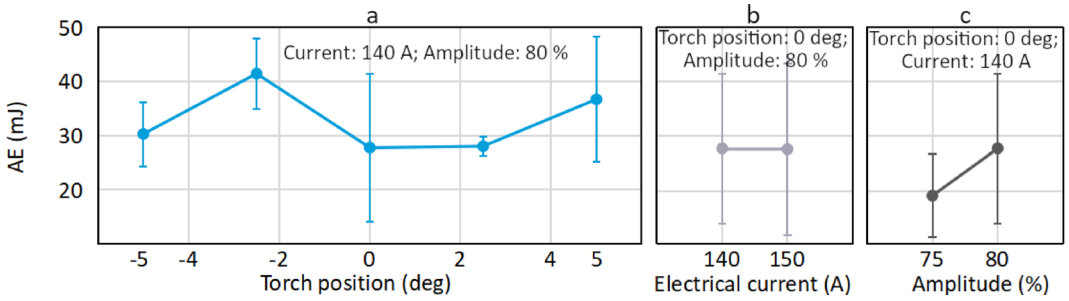

Fig. 8. AE of AlSi12 UA powder at varying arc manipulator (torch) angles (**a**), electrical currents (**b**), and vibration amplitudes (**c**).

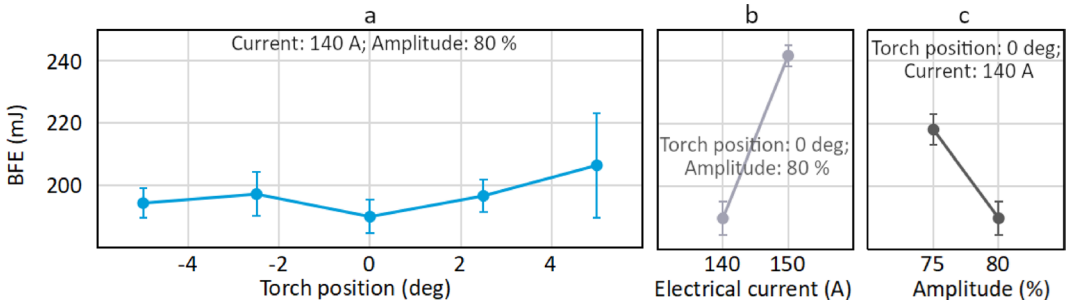

Fig. 9. AE of AlSi12 UA powder at varying arc manipulator (torch) angles (**a**), electrical currents (**b**), and vibration amplitudes (**c**).

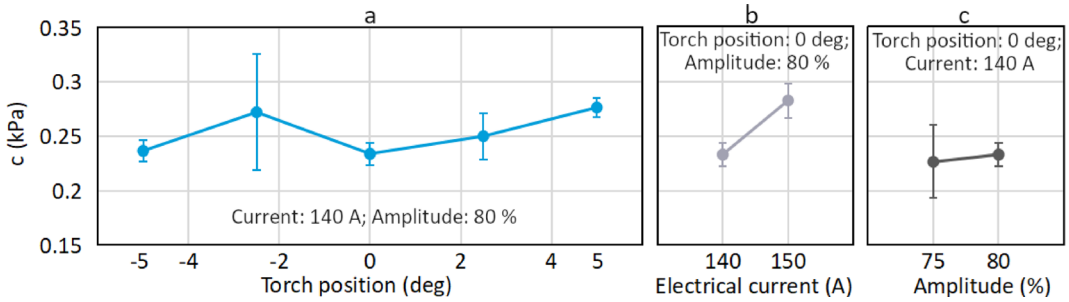

Fig. 10. AE of AlSi12 UA powder at varying arc manipulator (torch) angles (**a**), electrical currents (**b**), and vibration amplitudes (**c**).

larger variations than CBD, with changes reaching up to 31%, highlighting its greater sensitivity to UA process parameters compared to CBD.

The permeability test evaluated the ease with which a powder bed releases entrapped air by measuring the PD throughout the process. As shown in Fig. 6, PD does not exhibit a strong dependence on torch angle. Initially, PD decreases from −5 to 0 degrees, then rises slightly between 0 and 2.5 degrees, before declining again from 2.5 to 5 degrees, fluctuating within a range of 2.36 to 2.62 mBar (Fig. 6a). Increasing the current from 140 to 150 A causes PD to rise from 2.36 to 2.49 mBar (Fig. 6b), while reducing the amplitude from 80 to 75% leads to an insignificant increase in PD from 2.36 to 2.47 mBar (Fig. 6c). Overall, all variations in PD remain within a modest 10% range, indicating limited sensitivity to the tested UA parameters.

The SE measures the energy required to displace powder during upward blade movement, reflecting mechanical interlocking of particles. Overall, the SE gauges powder flowability in unconfined conditions[53,54]. According to the results, SE exhibits a similar trend to CI (Fig. 7); however, a decrease in amplitude from 80 to 75% increases SE, contrasting with CI, which remains unaffected by this change (Fig. 7c). The lowest SE value of approximately 3.01 mJ/g is observed at 140 A of current, 80% amplitude, and 0 degrees of angle, while the highest SE value of 4.09 mJ/g occurs under 150 A of current, 80% amplitude, and 0 degrees. This range, representing a significant 26.5% variation, highlights the higher sensitivity of SE to process parameters.

The aeration test evaluates how air addition influences powder behavior by comparing movements before and after aeration, with AE as the resulting output. Figure 8 shows that the mean values of AE can vary significantly, ranging from a minimum of 19.1 mJ to a maximum of 41.4 mJ, reflecting a change of over 50%. However, a closer examination reveals considerable data scatter, indicated by large standard deviations, which hinders the ability to draw definitive conclusions about specific trends or patterns. Therefore, the authors suggest that the UA parameters studied do not have a substantial effect on the AE, as the variability in the data overshadows any potential influence of these parameters.

The BFE is the energy required to move a specific powder volume and is qualitatively assessed during the seventh cycle of the stability and flow rate tests[54]. The BFE exhibits a correlation with the SE, reflecting similar trends and patterns. However, BFE demonstrates a narrower variation range, with a slower variation of 21.4%, ranging from 189.9 mJ to 241.5 mJ (Fig. 9). Additionally, no statistically significant trend is observed with increasing torch angle.

Finally, the cohesion coefficient (c) values were determined from the shear test, which evaluates the shear stresses required to initiate powder flow under consolidated conditions. Figure 10 illustrates that the c values vary by 15.4%, ranging from 0.234 to 0.276 kPa, as the arc manipulator angle changes. While the vibrating amplitude has a negligible effect on the c values (Fig. 10c), electrical current significantly influences them, increasing c from 0.234 to 0.283 kPa (Fig. 10b). The total range is about 19.6%.

All rheological results are summarized in Table 2. Increases in all rheological parameters, except for the CBD, indicate a decline in powder quality, whereas an increase in CBD suggests an improvement. It is evident

Rheological property	Increasing torch angle (−5 -> 5 deg)	Increasing electrical current (140 -> 150 A)	Increasing vibrating amplitude (75 -> 80%)
CBD	Decreases by 10% (1.064 -> 0.957 g/cm^3)	Decreases by 4% (1.017 -> 0.974 g/cm^3)	No clear trend
CI	Increases beyond 0 deg by 23.5% (2.73 -> 3.57%)	Increases by 31% (2.73% -> 3.94%)	No clear trend
PD	No clear trend	Increases by 5% (2.36 -> 2.49 mBar)	No clear trend
SE	Increases beyond 0 deg by 17% (3.01 -> 3.64 mJ/g)	Increases by 26% (3.01 -> 4.09 mJ/g)	Decreases by 14% (3.52 -> 3.01 mJ/g)
AE	No clear trend	No clear trend	No clear trend
BFE	No clear trend	Increases by 21% (189.9 -> 241.5 mJ)	Decreases by 13% (218.0 -> 189.9 mJ)
c	No clear trend	Increases by 17% (0.234 -> 0.283 kPa)	No clear trend

Table 2. Summary of rheological test results.

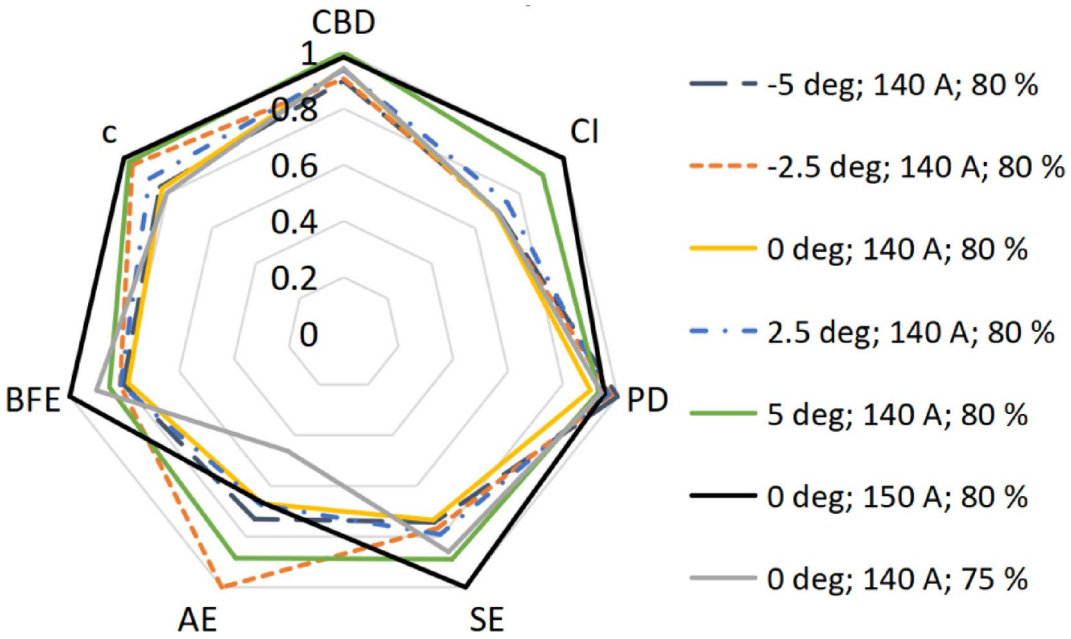

Fig. 11. Spider plot (radar diagram) showing various rheology indices for different AlSi12 UA powders under varying process parameters: (**a**) electrical currents and vibration amplitudes, (**b**) arc manipulator angles, and (**c**) overall comparison.

that increasing the electrical current from 140 A to 150 A leads to either inferior or comparable rheological properties: values of CI, PD, SE, BFE, and 'c' increased, AE remained unchanged, and CBD decreased. A similar trend is observed when the vibration amplitude is reduced from 80 to 75%. Regarding the arc manipulator angle, powder quality worsens as the angle increases from − 5° to 5°.

Additionally, the electrical current seems to be the most influential process parameter, as its variation resulted in the most substantial changes in 4 out of the 7 rheological parameters — namely, CI, SE, BFE, and c (see Table 2). The torch angle can be ranked as the second most impactful factor, significantly affecting 3 out of 7 parameters. While its influence on CI and SE was slightly less pronounced compared to that of the current, it exerted a stronger effect on CBD. In contrast, the vibrating amplitude demonstrated the least influence, causing only variations in 2 rheological parameters, with changes confined within a range of approximately 14%.

For comparison, all rheological parameters were normalized to their maximum values across the 7 powders, with the CBD parameter first being inverted before normalization. The resulting normalized values were then used to create a radar chart (spider plot) for all powders, as depicted in Fig. 11. This chart effectively highlights the performance of the powders under various UA process settings across multiple rheological parameters, where smaller values indicate better suitability for the AM process.

The charts reveal several notable trends. The UA settings of 0 degrees torch angle, 140 A current, and 80% amplitude consistently yield compact radar shapes, indicating a balanced and superior rheological profile across most parameters, especially in terms of lower BFE and SE. Settings with − 5 degrees and − 2.5 degrees torch angles also perform well, showing trade-offs between different parameters (e.g., improved bulk density). Conversely, the setting with 0 degrees and increased current of 150 A exhibits notably worse performance, particularly in CI, BFE, and SE, confirming the worse flowability and compressibility.

Modified additive manufacturing suitability factor

To quantify the processability of AM, Brika et al.[16] introduced a metric known as the Additive Manufacturing Suitability (AMS) factor (Eq. 2).

$$\mathrm{AMS} = \left(\frac{1}{\mathrm{CBD}} + \mathrm{CI} + \mathrm{PD} + \mathrm{SE} + \mathrm{AE} + \mathrm{BFE} + \mathrm{c}\right) / 7 \tag{2}$$

In this equation, all parameters are normalized according to their maximum values among all tested powders. Notably, the CBD is multiplicatively inversed and then normalized. It is also crucial to emphasize that while each parameter in Eq. 2 holds an equal weight of 1/7, adjusting the weighting factors can offer advantages in different scenarios[55].

Combining all the aforementioned considerations into a unified perspective, the AMS with weighting factors (w) can be reformulated as Eq. 3.

$$\mathrm{AMS_k} = \sum_{\mathrm{n=1}}^{\mathrm{N}} \mathrm{w_n} \times \frac{\mathrm{P_{kn}}}{\max\{\mathrm{P_{1n}}, \mathrm{P_{2n}}, \ldots \mathrm{P_{Kn}}\}} \tag{3}$$

where k = 1,…,K represents the number of powders analyzed, n = 1,…,N denotes the number of parameters utilized for comparative analysis, and $\mathrm{P_{kn}}$ signifies a parameter (such as CBD, CI, PD, etc.).

It is crucial to note that Eq. 3 can sometimes yield contentious outcomes. To illustrate this, consider two powders — Powder 1 and Powder 2 — with the following parameter values: Par.1 is 1 for Powder 1 and 2 for Powder 2, while Par.2 is 3 for Powder 1 and 2 for Powder 2 (see Fig. 12). For simplicity, both parameters are given equal weight. After applying normalization and calculating the AMS score, Powder 1 appears to be superior, with an AMS of 0.75 compared to 0.83 for Powder 2. However, when a third powder (Powder 3) is introduced into the comparison, the results change. As shown in Fig. 12, the AMS scores shift such that Powder 2 now appears better than Powder 1, with AMS values of 0.55 and 0.43, respectively. This example demonstrates how the addition of a new option can unexpectedly alter the relative rankings of the original powders.

This discrepancy arises because the relationship between $\mathrm{AMS_1}$ and $\mathrm{AMS_2}$ at k = 2 may not necessarily mirror that at k = 3, given that the denominator of Eq. 3 ($\max\{\mathrm{P_{1n}},\ldots,\mathrm{P_{Kn}}\}$) could change with the inclusion of a new powder. In the example provided, the values of Parameter 1 for Powder 1 and Powder 2 are much smaller than those of the newly introduced Powder 3 (with Par.1 = 1 for Powder 1, 2 for Powder 2, and 10 for Powder 3). As a result, after normalization, the first parameter for Powders 1 and 2 becomes close to zero. This diminishes the influence of Parameter 1 and increases the impact of Parameter 2 on the AMS calculation.

However, the model's purpose is to yield consistent outcomes regardless of the quantity of powders considered. To address this issue, we can implement a logarithmic transformation 4.

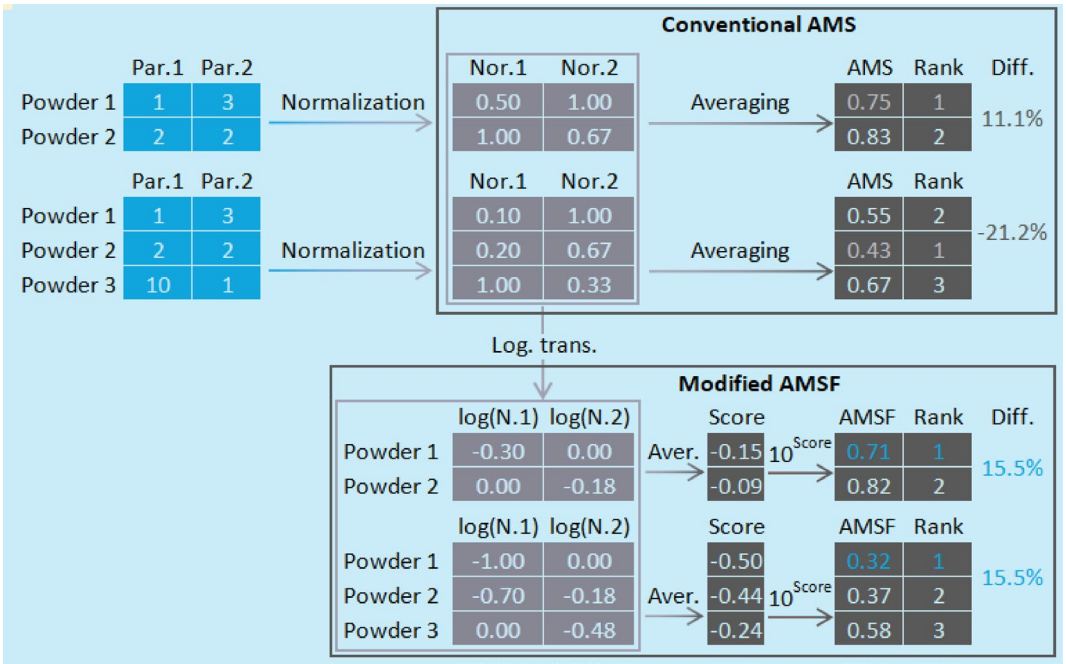

Fig. 12. Comparison of the controversial results from the conventional AM suitability factor versus the consistent outcomes of the modified version.

$$\sum_{n=1}^{N} w_n \times \log \frac{P_{kn}}{\max\{P_{1n}, P_{2n}, \ldots P_{Kn}\}} \tag{4}$$

While AMS ranges from 0 to 1, the transformation (4) spans from -∞ to 0. To standardize it with the range of Eq. 3, let's elevate (4) to the 10th power. After all transformations, the modified AMS can be expressed as Eq. 5.

$$AMSF_k = \prod_{n=1}^{N} \left(\frac{P_{kn}}{\max\{P_{1n}, P_{2n}, \ldots P_{Kn}\}} \right)^{w_n} \tag{5}$$

Now, when using Eq. 5, the relationship between $AMSF_1$ and $AMSF_2$ remains consistent regardless of whether k = 2 or k = 3. This consistency occurs because the denominator term ($\max\{P_{1n},\ldots,P_{Kn}\}$) cancels out during the division, ensuring that relative differences are preserved. As shown in Fig. 12, $AMSF_1$ is 15.5% lower than $AMSF_2$ in both cases.

Weighting factors could vary depending on the situation; for instance, in scenarios involving prolonged cyclic loading, parameters affecting fatigue resistance might carry greater significance (assigned a higher weight). Similarly, in scenarios focusing on corrosion protection, parameters influencing corrosion resistance would be prioritized.

When there is no clear understanding of the relationships between powder parameters and the desired behavior of printed parts, parameter weights can be determined based on the accuracy of their measurement. Parameters with higher coefficients of variation should have less impact on the resulting AMS values and thus be assigned smaller weighting factors, thereby reducing the influence of parameters with greater uncertainty. The formula used to calculate these weights is provided in Eq. 6.

$$w_n = \frac{1}{CV_n \times \sum_{i=1}^{N} (1/CV_i)} \tag{6}$$

where CV_n denotes the coefficient of variation for the n^{th} parameter.

Weighting factors for CBD, CI, PD, SE, AE, BFE, and 'c' were calculated based on the median values of coefficients of variation for the rheological parameters derived from an extensive literature review (see Yankin et al.[40]). Specifically, the weighting factors were 0.54 for CBD, 0.1 for CI, 0.1 for PD, 0.11 for SE, 0.02 for AE, 0.11 for BFE, and 0.02 for 'c'.

It is also worth noting that the paper[40] includes key descriptive statistics such as the median, quartiles, maximum, and minimum values. This allows authors to review their experimental data, particularly to identify whether any CVs are outliers, which would be indicated if they are above the maximum or below the minimum values. If any CVs are identified as outliers, it is advisable to consider rerunning tests for those parameters. Statistic values for some rheological parameters are presented in Table 3.

Therefore, the presented approach enables the formulation of a unified methodology for conducting a comparative analysis of two or more similar powders, based on specific parameters. The method is implemented using Jupyter + Python or MS Excel software, available on GitHub: https://github.com/yanicen1/Additive-Manufacturing-Suitability-Factor.

Figure 13 presents the results of the AMSF application, highlighting minor fluctuations of less than 1.5% in AMSF values, ranging from 0.823 to 0.836, as the torch angle shifts from −5 to 0 degrees. Beyond this, a steady increase in AMSF values is observed, rising from 0.829 to 0.924 as the torch angle changes from 0 to 5 degrees (Fig. 13a). Notably, when the torch angle decreases, the droplets form and fly away at a lower angle relative to the platform, positioning them farther from the electric arc. Conversely, when the torch angle increases, the droplets are closer to the arc. We hypothesize that this positioning likely exposes the droplets to additional heat from the electric arc, potentially causing secondary melting and deterioration of their properties and overall powder quality, as observed in Fig. 13.

An increase in electrical current leads to higher AMSF values, indicating a decline in suitability (Fig. 13b). Specifically, when the current is raised from 140 A to 150 A, the AMSF increases from 0.829 to 0.943. Overall, selecting the appropriate current is vital for achieving optimal melting conditions. Excessively high values can overheat the material, adversely affecting the atomization process. That is what was observed in the study, with a noticeable deterioration in powder quality when exposed to elevated current levels.

	Coefficients of Variation						
	CBD	CI	PD	SE	AE	BFE	c
max	1.90	16.18	11.54	15.67	75.82	10.42	50.00
Q3	1.30	8.02	6.31	7.12	37.21	5.42	25.97
median	0.65	3.67	3.41	3.25	21.55	3.18	16.91
Q1	0.36	1.52	2.02	1.34	10.41	1.84	6.47
min	0.04	0.52	0.26	0.16	5.15	0.59	2.80

Table 3. Descriptive statistics of CVs for the rheological parameters.

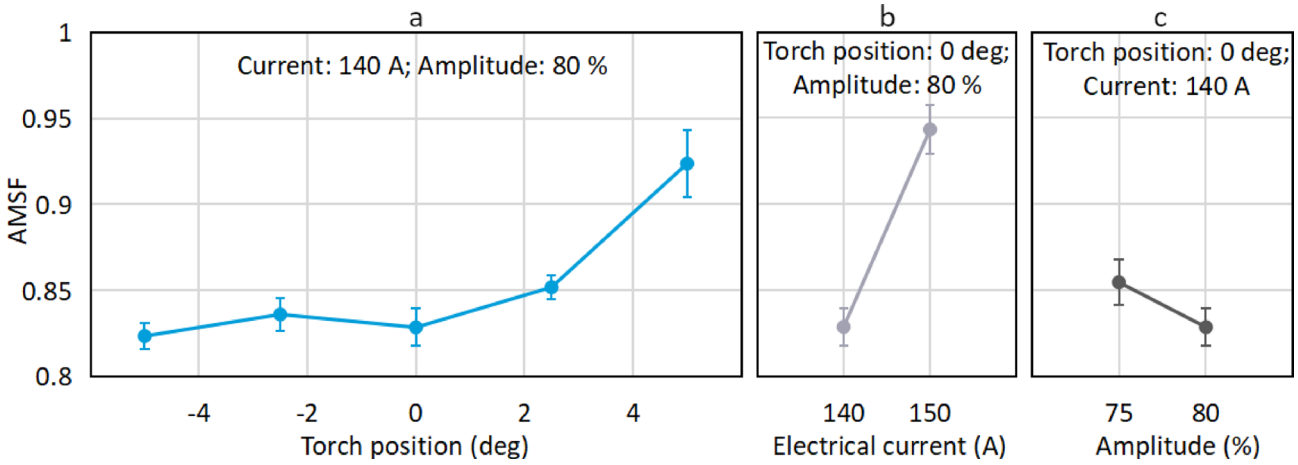

Fig. 13. AMSF for different AlSi12 UA powders at varying arc manipulator angles (**a**), electrical currents (**b**), and vibration amplitudes (**c**).

A reduction in vibrating amplitude results in higher AMSF values, indicating worsened suitability. Specifically, when the amplitude drops from 80 to 75%, the AMSF increases from 0.829 to 0.854 (Fig. 13c). Overall, adjusting the amplitude is essential for optimizing atomization efficiency; higher amplitudes improve efficiency, while lower values can halt the atomization process entirely. However, amplitude likely has a less significant impact on powder quality compared to other factors, such as electrical current or torch position.

The best AMSF values were observed in powders with torch positions of −5 and 0 degrees, combined with 140 A of current and 80% amplitude. The powder at 0 degrees torch angle was only 0.6% worse than that at −5 degrees.

To enhance the robustness of the conclusions, an additional statistical analysis was performed. Specifically, a regression model was applied to the experimental data presented in Fig. 13. A similar methodology has been employed in previous study[56]. In this analysis, the three input variables were torch angle (Tor), electrical current (El.Cur), and vibration amplitude (Amp), with AMSF serving as the output variable. Given the observed non-linear relationship between AMSF and torch angle, a polynomial regression model was considered, as described by Eq. (7). Before determining the model coefficients, the input variables were standardized to enable direct comparison of their effects.

$$\mathrm{AMSF_{pr}} = 0.8659 + 0.039 \cdot \mathrm{El.\ Cur} - 0.0082 \cdot \mathrm{Amp} + 0.0259 \cdot \mathrm{Tor} + 0.0179 \cdot \mathrm{Tor}^2 \quad (7)$$

The resulting model demonstrated an adjusted R^2 value of 0.862, an F-statistic of 32.18 (p-value = 1.81×10^{-7}), and a root mean square error (RMSE) of 0.016. For reference, the experimental error ranges from 0.007 to 0.019. These results indicate that the regression model provides a reliable fit to the data. As shown in Eq. (7), the electrical current has the largest coefficient (0.039), followed by the torch angle (0.0259), the squared torch angle term (0.0179), and amplitude (0.0082). Thus, among the parameters, electrical current and torch angle have the strongest influence on AMSF, while amplitude has the least.

Comparative analysis of UA and commercial powders

This study incorporates a commercial AlSi12 powder for comparative analysis, alongside the best (No. 4 from Table 1) and worst (No. 3 from Table 1) UA powder samples identified in the previous section. The best UA powder was obtained using process parameters of 140 A electrical current, 80% vibrating amplitude, and a torch position of −5 degrees. The worst UA powder was produced with 150 A electrical current, 80% vibrating amplitude, and a torch position of 0 degrees. The commercial powder used was CL 30AL aluminium alloy powder (AlSi12), specifically engineered for AM applications. This reactive powder material conforms to the chemical composition standards of DIN EN 1706, ensuring reliable and consistent material properties. The shape and size distribution of the powder particles are tailored to optimize performance for the technology and the process. Notably, the commercial powder was used as received, without any additional sieving.

Figure 14 presents the PSD metrics (D_{10}, D_{50}, D_{90}, and span) for the three powders. The commercial powder exhibits significantly smaller particle sizes compared to both UA powders, as indicated by its notably lower D_{10}, D_{50}, and D_{90} values. Despite the finer particles, the commercial powder shows a broader size distribution, with a span approximately 72% higher than that of the best UA powder and 59% higher than the worst UA powder.

Figure 15 shows SEM images that visually support the PSD results, highlighting differences in particle morphology among the powders. The commercial AlSi12 powder displays highly irregular particle shapes, characterized by elongated and non-spherical forms. Additionally, many particles exhibit some satellite particles fused to their surfaces. Overall, the commercial powder demonstrates a significantly poorer morphology compared to the UA powders.

Figure 16 presents the rheological results, highlighting the following findings: The commercial powder's CBD is slightly higher, being 2.7% better than the best UA powder and 11.0% better than the worst UA powder.

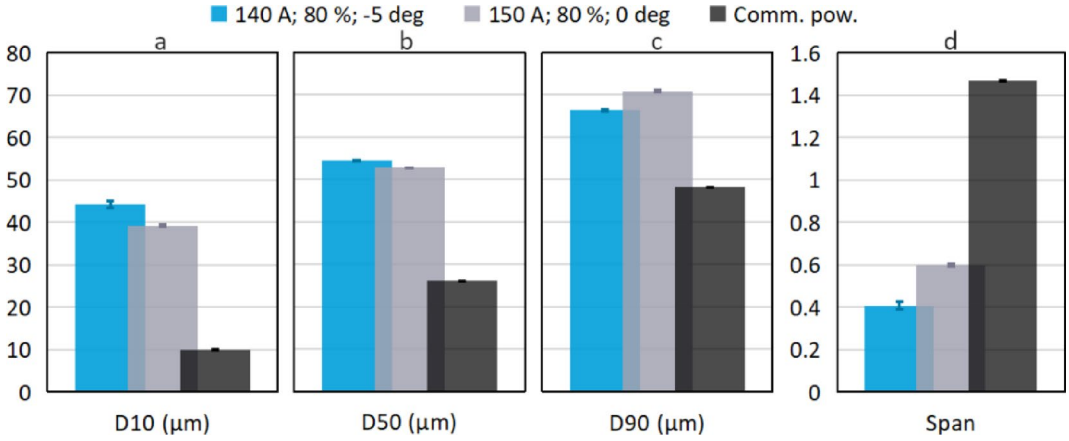

Fig. 14. Comparative analysis of D_{10} (**a**), D_{50} (**b**), D_{90} (**c**), and S (**d**) parameters between the best (140 A, 80%, −5 deg) and worst (150 A, 80%, 0 deg) AlSi12 UA powder samples and a commercial equivalent.

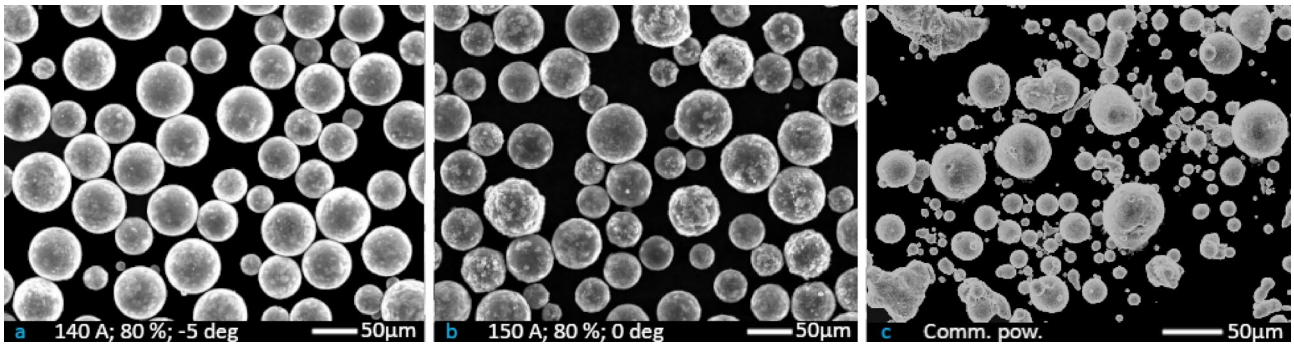

Fig. 15. SEM micrographs comparing AlSi12 UA powder samples under different conditions: (**a**) the best sample processed at 140 A, 80%, and −5 deg; (**b**) the worst sample processed at 150 A, 80%, and 0 deg; and (**c**) a commercial AlSi12 powder for reference.

However, the CI of the commercial powder is significantly worse, showing values 45.1% and 21.6% higher compared to the best and worst UA powders, respectively. The PD of the commercial powder is markedly worse, with 84.9% and 85.6% compared to the best and worst UA powders. The SE parameter is 22.8% worse for the commercial powder compared to the best UA powder but shows similar values to the worst UA powder. No significant differences were observed in the AE among the three powders due to high standard deviations. The BFE of the commercial powder is 22.4% and 37.6% better than the best and worst UA powders, respectively. Finally, the *c* parameter of the commercial powder is comparable to that of the best UA powder and 23.5% better than that of the worst UA powder.

Overall, the best UA powder (produced at 140 A, 80%, and −5 degrees) outperforms the commercial powder in 3 out of 7 rheological parameters, shows similar results in 2 parameters, and performs worse in 2 parameters. Importantly, in the two instances where the UA powder underperforms (CBD and BFE), the differences are relatively small — 2.7% and 22.4%, respectively. In contrast, the UA powder shows substantially better performance in the three parameters where it excels, with improvements of 45.1%, 84.9%, and 22.8% for CI, PD, and SE, respectively.

The normalized rheological properties of the powders are illustrated in a spider plot, as shown in Fig. 17. This visualization allows for a direct comparison of the performance between the UA and commercial powders across various rheological parameters. In addition to this, Fig. 17 also presents the results of the AMSF calculations for all three powders under evaluation.

The AMSF results clearly indicate that the commercial powder performs the poorest compared to both UA powders, with an AMSF value of 0.825. In contrast, the best-performing UA powder achieved an AMSF of 0.653, while the worst UA powder had an AMSF of 0.747. Hereby, the commercial powder's AMSF is approximately 21% worse than that of the best UA powder and 9.5% worse than that of the worst UA powder.

The performance gap between the best and worst UA powders remains consistent at 12.7%, regardless of the inclusion or exclusion of specific powder samples. This consistency is attributed to the modified methodology of AMSF, as detailed in Sect. Modified additive manufacturing suitability factor. This methodology ensures robust and stable outcomes when comparing powder samples across multiple metrics.

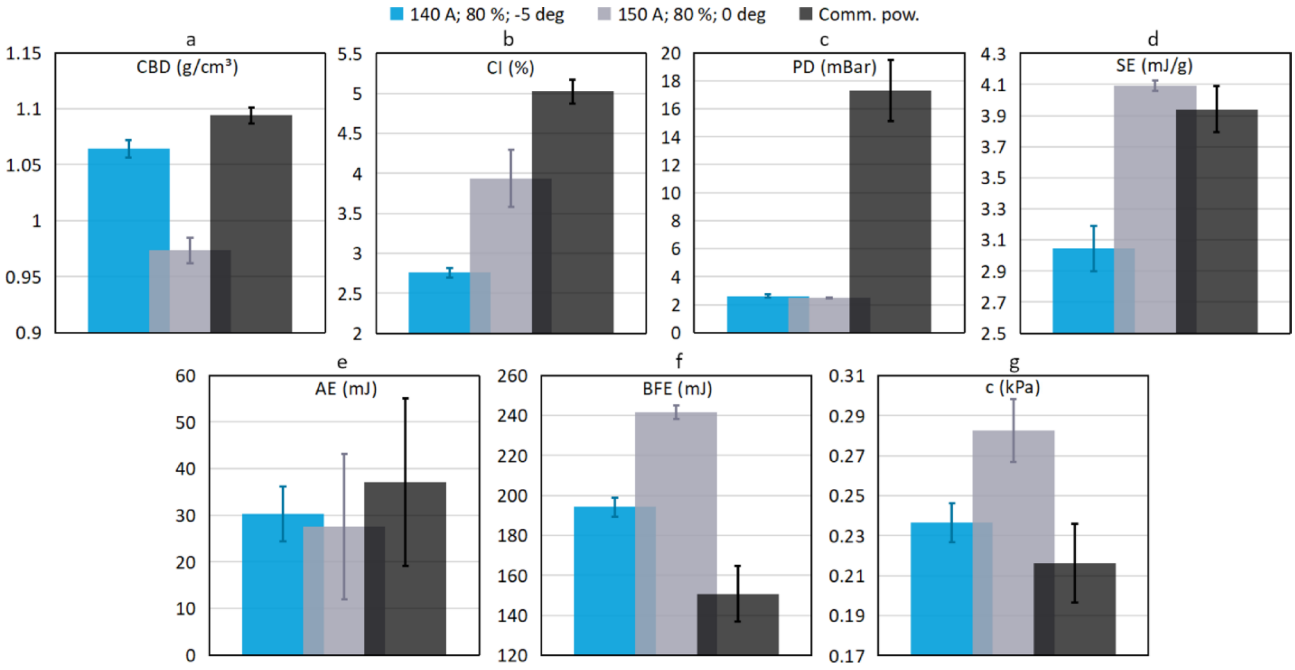

Fig. 16. Comparative analysis of rheological properties between the best (140 A, 80%, −5 deg) and worst (150 A, 80%, 0 deg) AlSi12 UA powder samples and a commercial equivalent: CBD (**a**), CI (**b**), PD (**c**), SE (**d**), AE (**e**), BFE (**f**), and *c* (**g**).

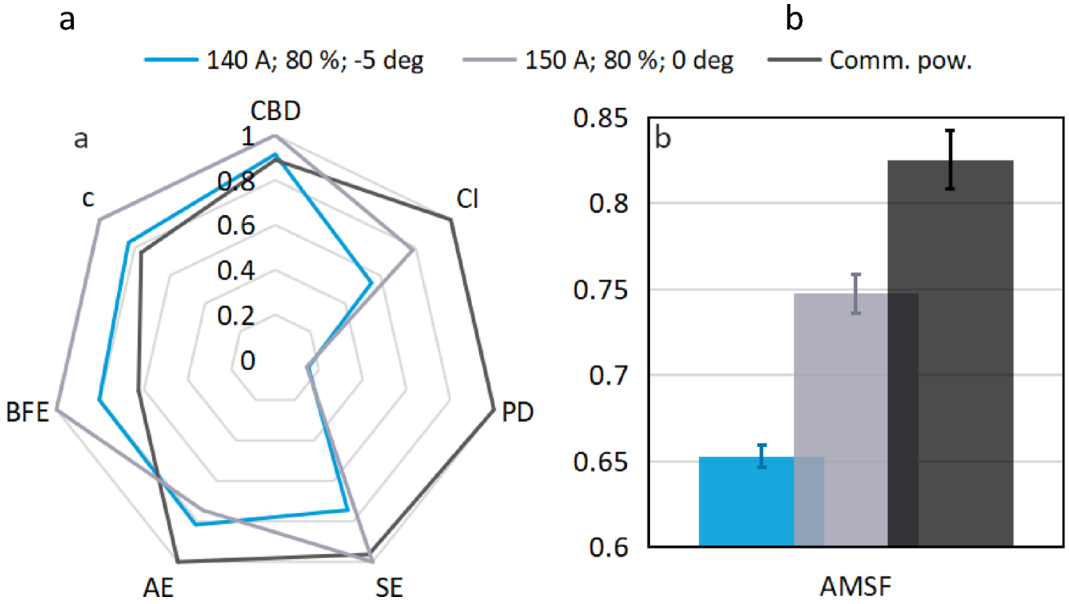

Fig. 17. Comparative diagrams of spider plot (**a**) and AMSF (**b**) for the best (140 A, 80%, −5 deg) and worst (150 A, 80%, 0 deg) AlSi12 UA powder samples, compared to a commercial equivalent.

Conclusions

This novel study investigated the effects of process parameters on the quality of AlSi12 powder produced using an advanced ultrasonic atomization technique, addressing key gaps in the literature on optimizing powder characteristics. The research also included a comparative analysis of in-house ultrasonically atomized powders and a commercial counterpart. Key findings from the study are as follows:

- Adjusting process parameters, such as the electric arc manipulator angle, electrical current, and vibrating amplitude, significantly affects particle size distribution, which can impact powder flow and packing ability. While distribution parameters D_{10}, D_{50}, and D_{90} exhibit moderate variations of up to 13.5%, the span shows

a more pronounced difference of up to 37.5%. The span remains steady at ~ 0.4 from − 5 to −2.5 degrees, rises to 0.5 between − 2.5 and 0 degrees, and stabilizes. Increasing the current to 150 A raises the span to 0.6, while reducing vibration amplitude increases it statistically insignificantly.

- Changes in arc manipulator angle from − 5 to 5 degrees, increasing electrical current, and decreasing vibrating amplitude generally worsen rheological properties. Certain parameters, such as the compressibility index, specific energy, and basic flow energy, are highly sensitive, showing up to 30% variability, while others, like conditioned bulk density and pressure drop, are less affected, with around 10% variability. Some properties, such as aeration energy, are largely independent of these parameters.
- During the powder quality estimation, it was revealed that the traditional additive manufacturing suitability factor sometimes led to contradictory results due to the inclusion of different numbers of powder types in the analysis. To resolve this problem, a modified approach was developed that implements logarithmic transformations and custom weighting factors. This methodology ensures consistent results regardless of the number of powders considered in the analysis. Additionally, the maximum-minimum value ranges for the coefficients of variation of rheological parameters were demonstrated to identify outliers during testing.
- The arc manipulator angle alters the trajectory of formed droplets, affecting how they interact with the electric arc. Non-linear changes in powder performance are observed, with total quality significantly deteriorating when the angle moves beyond 0 to 5 degrees. However, at angles of 0 degrees or less, no significant impact on powder quality was detected. Increasing electrical current and reducing vibrating amplitude also harm powder suitability for additive manufacturing.
- Electrical current was identified as the most influential factor on powder suitability for additive manufacturing, causing a 12.7% variation. The arc manipulator angle followed, contributing to a 10.9% change, while vibrating amplitude had the least impact, with only a 3.6% change.
- The commercial powder performed the worst compared to all ultrasonically atomized powders, with its suitability factor being approximately 21% worse than the best ultrasonically atomized powder and 9.5% lower than the worst.
- The ultrasonically atomized AlSi12 powders exhibited highly spherical and uniform particles with minimal satellite particles, contrasting sharply with the commercial powder, which displayed irregular, elongated shapes and particle fusion. Overall, the commercial powder showed significantly poorer morphology compared to the ultrasonically atomized samples.

Data availability

All data generated or analysed during this study are included in this published article.

Received: 27 March 2025; Accepted: 5 June 2025
Published online: 01 July 2025

References

1. Dada, M. & Popoola, P. Recent advances in joining technologies of aluminum alloys: a review. *Discover Mater.* **4**, https://doi.org/10.1007/s43939-024-00155-w (2024).
2. Kurek, M. Fatigue prediction of aluminum alloys considering critical plane orientation under complex stress States. *Materials* **13**, 3877. https://doi.org/10.3390/ma13173877 (2020).
3. Yankin, A., Lykova, A., Mugatarov, A., Wildemann, V. & Ilinykh, A. Influence of additional static stresses on biaxial low-cycle fatigue of 2024 aluminum alloy. *Frattura Ed. Integrità Strutturale*. **16**, 180–193. https://doi.org/10.3221/IGF-ESIS.62.13 (2022).
4. Pan, C-C. et al. Enhancing the cavitation erosion resistance of additive manufactured Al-Si alloys with strong connective Si networks. *J. Mater. Sci. Technol.* https://doi.org/10.1016/j.jmst.2025.02.006 (2025).
5. Yankin, A., Seisekulova, A., Perveen, A. & Talamona, D. Mechanical properties of additively manufactured AlSi10Mg under quasi-static and Cyclic loading. *Fatigue Fract. Eng. Mater. Struct.* **47**, 1696–1714. https://doi.org/10.1111/ffe.14263 (2024).
6. Kekana, N., Shongwe, M. B., Mpofu, K. & Muvunzi, R. A review on factors influencing mechanical properties of AlSi12 alloy processed by selective laser melting. *Int. J. Adv. Manuf. Technol.* **121**, 4313–4323. https://doi.org/10.1007/s00170-022-09582-6 (2022).
7. Blakey-Milner, B. et al. Du plessis, metal additive manufacturing in aerospace: A review. *Mater. Design*. **209**, 110008. https://doi.org/10.1016/j.matdes.2021.110008 (2021).
8. Gradl, P. et al. Robust metal additive manufacturing process selection and development for aerospace components. *J. Materi Eng. Perform*. **31**, 6013–6044. https://doi.org/10.1007/s11665-022-06850-0 (2022).
9. Tuncer, N., Bose, A., Manufacturing, S. S. M. A. & Review, A. *JOM* **72** 3090–3111. https://doi.org/10.1007/s11837-020-04260-y (2020).
10. Strondl, A., Lyckfeldt, O., Brodin, H. & Ackelid, U. Characterization and control of powder properties for additive manufacturing. *JOM* **67**, 549–554. https://doi.org/10.1007/s11837-015-1304-0 (2015).
11. Wang, S., Tao, S. & Peng, H. Influence of powder characteristics on the microstructure and mechanical behaviour of GH4099 Superalloy fabricated by Electron beam melting. *Metals* **12**, 1301. https://doi.org/10.3390/met12081301 (2022).
12. Seyda, V., Herzog, D. & Emmelmann, C. Relationship between powder characteristics and part properties in laser beam melting of Ti–6Al–4V, and implications on quality. *J. Laser Appl.* **29**, https://doi.org/10.2351/1.4983240 (2017).
13. Young, Z. et al. Effects of particle size distribution with efficient packing on powder flowability and selective laser melting process. *Materials* **15**, 705. https://doi.org/10.3390/ma15030705 (2022).
14. Zhang, J. et al. A computer vision approach to evaluate powder flowability for metal additive manufacturing. *Integr. Mater. Manuf. Innov.* **10**, 429–443. https://doi.org/10.1007/s40192-021-00226-3 (2021).
15. Averardi, A., Cola, C., Zeltmann, S. E. & Gupta, N. Effect of particle size distribution on the packing of powder beds: A critical discussion relevant to additive manufacturing. *Mater. Today Commun.* **24**, 100964. https://doi.org/10.1016/j.mtcomm.2020.100964 (2020).
16. Brika, S. E., Letenneur, M., Dion, C. A. & Brailovski, V. Influence of particle morphology and size distribution on the powder flowability and laser powder bed fusion manufacturability of Ti-6Al-4V alloy. *Additive Manuf.* **31**, 100929. https://doi.org/10.1016/j.addma.2019.100929 (2020).
17. Li, J. et al. Particle size dependence of the microsegregation and microstructure in the atomized Ni-based Superalloy powders: theoretical and experimental study. *J. Mater. Sci. Technol.* **171**, 54–65. https://doi.org/10.1016/j.jmst.2023.07.006 (2024).

18. Yim, S., Bian, H., Aoyagi, K., Yamanaka, K. & Chiba, A. Effect of powder morphology on flowability and spreading behavior in powder bed fusion additive manufacturing process: A particle-scale modeling study. *Additive Manuf.* **72**, 103612. https://doi.org/10.1016/j.addma.2023.103612 (2023).
19. Henein, H., Uhlenwinkel, V. & Fritsching, U. (eds), Metal Sprays and Spray Deposition, Springer International Publishing, (2017). https://doi.org/10.1007/978-3-319-52689-8
20. Seyam, M. S., Koshy, P. & Elbestawi, M. A. Laser powder bed fusion of unalloyed tungsten: A review of process, structure, and properties relationships. *Metals* **12**, 274. https://doi.org/10.3390/met12020274 (2022).
21. Kassym, K. & Perveen, A. Atomization processes of metal powders for 3D printing. *Mater. Today: Proc.* **26**, 1727–1733. https://doi.org/10.1016/j.matpr.2020.02.364 (2020).
22. Singh, S., Ramakrishna, S. & Singh, R. Material issues in additive manufacturing: A review. *J. Manuf. Process.* **25**, 185–200. https://doi.org/10.1016/j.jmapro.2016.11.006 (2017).
23. Shi, Y. et al. Impact of gas pressure on particle feature in Fe-based amorphous alloy powders via gas atomization: simulation and experiment. *J. Mater. Sci. Technol.* **105**, 203–213. https://doi.org/10.1016/j.jmst.2021.06.075 (2022).
24. Asgarian, A., Tang, Z., Bussmann, M. & Chattopadhyay, K. Water atomisation of metal powders: effect of water spray configuration. *Powder Metall.* **63**, 288–299. https://doi.org/10.1080/00325899.2020.1802558 (2020).
25. Wang, L. et al. Atomization gases dependent mechanical properties in the laser powder bed fusion manufactured 304L stainless steel. *J. Mater. Process. Technol.* **316**, 117966. https://doi.org/10.1016/j.jmatprotec.2023.117966 (2023).
26. Luo, S. et al. The impact of coaxial gas technology on the morphology of powder by gas atomisation and the additive manufactured mechanical performance. *Virtual Phys. Prototyp.* 19. https://doi.org/10.1080/17452759.2024.2375107 (2024).
27. Zhang, K. et al. Pore evolution mechanisms during directed energy deposition additive manufacturing. *Nat. Commun.* 15. https://doi.org/10.1038/s41467-024-45913-9 (2024).
28. Brewin, P. R., Walker, P. I. & Nurthen, P. D. Production of high alloy powders by water atomization. *Powder Metall.* **29**, 281–285. https://doi.org/10.1179/pom.1986.29.4.281 (1986).
29. Priyadarshi, A. et al. New insights into the mechanism of ultrasonic atomization for the production of metal powders in additive manufacturing. *Additive Manuf.* **83**, 104033. https://doi.org/10.1016/j.addma.2024.104033 (2024).
30. Żrodowski, Ł. et al. Novel cold crucible ultrasonic atomization powder production method for 3D printing. *Materials* **14**, 2541. https://doi.org/10.3390/ma14102541 (2021).
31. Lang, R. J. Ultrasonic atomization of liquids. *J. Acoust. Soc. Am.* **34**, 6–8. https://doi.org/10.1121/1.1909020 (1962).
32. Lierke, E. G. & Grießhammer, G. The formation of metal powders by ultrasonic atomization of molten metals. *Ultrasonics* **5**, 224–228. https://doi.org/10.1016/0041-624x(67)90066-2 (1967).
33. Bauckhage, K., Andersen, O., Hansmann, S., Reich, W. & Schreckenberg, P. Production of fine powders by ultrasonic standing wave atomization. *Powder Technol.* **86**, 77–86. https://doi.org/10.1016/0032-5910(95)03040-9 (1996).
34. Kustron, P. et al. Development of High-Power ultrasonic system dedicated to metal powder atomization. *Appl. Sci.* **13**, 8984. https://doi.org/10.3390/app13158984 (2023).
35. Wang, Z., Fabrication of al and al-Si alloy microspheres by ultrasonic irradiating the molten salt-aluminum immiscible system. *Ultrason. Sonochem.* **50**, 373–376. https://doi.org/10.1016/j.ultsonch.2018.09.039 (2019).
36. Pohlman, R., Heisler, K. & Cichos, M. Powdering aluminium and aluminium alloys by ultrasound. *Ultrasonics* **12**, 11–15. https://doi.org/10.1016/0041-624x(74)90080-8 (1974).
37. Shabana, S. et al. Improved synthesis of aluminium nanoparticles using ultrasound assisted approach and subsequent dispersion studies in di-octyl adipate. *Ultrason. Sonochem.* **36**, 59–69. https://doi.org/10.1016/j.ultsonch.2016.11.020 (2017).
38. JEDYNAK, A. Semi-finished powder of aluminum matrix composite for a direct energy deposition additive manufacturing. *Mater. Res. Proc.* **28**, 199–206. https://doi.org/10.21741/9781644902479-22 (2023).
39. Monti, C., Turani, M., Papis, K. & Bambach, M. A new Al-Cu alloy for LPBF developed via ultrasonic atomization. *Mater. Design.* **229**, 111907. https://doi.org/10.1016/j.matdes.2023.111907 (2023).
40. Yankin, A. et al. Comprehensive analysis of ultrasonically atomized 316L stainless steel powder using adjusted additive manufacturing suitability factor. *Powder Technol.* **444**, 120004. https://doi.org/10.1016/j.powtec.2024.120004 (2024).
41. Bałasz, B., Bielecki, M., Gulbiński, W. & Słoboda, Ł. Comparison of ultrasonic and other atomization methods in metal powder production. *J. Achievements Mater. Manuf. Eng.* **116**, 11–24. https://doi.org/10.5604/01.3001.0016.3393 (2023).
42. Andrich, D. The Rasch distribution: A discrete, general form of the Gauss distribution of uncertainty in scientific measurement. *Measurement* **173**, 108672. https://doi.org/10.1016/j.measurement.2020.108672 (2021).
43. Groarke, R. et al. Brabazon, 316L stainless steel powders for additive manufacturing: relationships of powder rheology, size, size distribution to part properties. *Materials* **13**, 5537. https://doi.org/10.3390/ma13235537 (2020).
44. Freeman, R. Measuring the flow properties of consolidated, conditioned and aerated powders — A comparative study using a powder rheometer and a rotational shear cell. *Powder Technol.* **174**, 25–33. https://doi.org/10.1016/j.powtec.2006.10.016 (2007).
45. Freeman, R. & Fu, X. Characterisation of powder bulk, dynamic flow and shear properties in relation to die filling. *Powder Metall.* **51**, 196–201. https://doi.org/10.1179/174329008x324115 (2008).
46. Basyir, A. B. A. et al. Investigation of effect of various hot gas atomisation and melting pot temperatures on Tin alloy powder product. *Sains Malaysiana.* **51**, 3027–3041. https://doi.org/10.17576/jsm-2022-5109-23 (2022).
47. Wisutmethangoon, S., Plookphol, T. & Sungkhaphaitoon, P. Production of SAC305 powder by ultrasonic atomization. *Powder Technol.* **209**, 105–111. https://doi.org/10.1016/j.powtec.2011.02.016 (2011).
48. Zhiwei Q. Improving gas flow in gas atomization. Degree project materials science and engineering, Second cycle, 30 Credits, Stockholm Sweden 2021.
49. Baskoro, A. S., Supriadi, S. & Dharmanto, N. Review on Plasma Atomizer Technology for metal powder. MATEC Web of Conferences. ; 269: 05004. (2019). https://doi.org/10.1051/matecconf/201926905004
50. Zhang, P., Yu, H., Wang, R., Sun, G., Bi, Z., & Zhang, S. Effect of particle surface roughness on the flowability and spreadability of Haynes 230 powder during laser powder bed fusion process. https://doi.org/10.2139/ssrn.4505099
51. Haferkamp, L. et al. The influence of particle shape, powder flowability, and powder layer density on part density in laser powder bed fusion. *Metals* **11**, 418. https://doi.org/10.3390/met11030418 (2021).
52. Chu, F. et al. Influence of satellite and agglomeration of powder on the processability of AlSi10Mg powder in laser powder bed fusion. *J. Mater. Res. Technol.* **11**, 2059–2073. https://doi.org/10.1016/j.jmrt.2021.02.015 (2021).
53. Ziegelmeier, S., Wöllecke, F., Tuck, C. & Goodridge, R. Characterizing the Bulk & Flow Behaviour of LS Polymer Powders, (2013). https://doi.org/10.26153/TSW/15437
54. Madian, A. et al. Impact of fine particles on the rheological properties of uranium dioxide powders. *Nuclear Eng. Technol.* **52**, 1714–1723. https://doi.org/10.1016/j.net.2020.01.012 (2020).
55. Habibnejad-korayem, M., Zhang, J. & Zou, Y. Effect of particle size distribution on the flowability of plasma atomized Ti-6Al-4V powders. *Powder Technol.* **392**, 536–543. https://doi.org/10.1016/j.powtec.2021.07.026 (2021).
56. Lobanov, D., Yankin, A. S. & Berdnikova, N. I. Statistical evaluation of the effect of hygrothermal aging on the interlaminar shear of GFRP. *Frattura Ed. Integrità Strutturale.* **16**, 146–157. https://doi.org/10.3221/IGF-ESIS.60.11 (2022).

Author contributions

Andrei Yankin: Writing – review & editing, Writing – original draft, Methodology, Investigation, Formal analy-

sis. Hussain Ali Murtaza: Investigation, Data curation. Boris Golman: Writing – review & editing, methodology, Conceptualization, Supervision Asma Perveen: Writing – review & editing, Supervision, Project administration, Methodology, Conceptualization. Didier Talamona: Writing – review & editing, Supervision, Resources, Funding acquisition.

Funding
This research was funded under the project "Design, fabrication & characterization of metal lattice structures using ultrasonically atomized powder" (grant no: 211123CRP1615) by Nazarbayev University.

Declarations

Competing interests
The authors declare no competing interests.

Ethics declarations
Not applicable.

Additional information
Correspondence and requests for materials should be addressed to D.T.

Reprints and permissions information is available at www.nature.com/reprints.

Publisher's note Springer Nature remains neutral with regard to jurisdictional claims in published maps and institutional affiliations.